BACHELOR

Measuring plasma dust removal using a high velocity centrifuge

Beckers, J.P.

Award date:
2015

Measuring plasma dust removal using a high velocity centrifuge

Jasper Beckers
EPG, Eindhoven University of Technology

June 26, 2015

Abstract

Dust particles can be removed from a surface by applying a plasma. The particles acquire a charge and are electromagnetically pulled away from the surface by the electric field in the plasma sheath. A method of measuring this plasma removal force is by determining the rotational velocity needed to release particles from a centrifuge. By comparing the forces needed with and without a plasma applied the plasma force can be found. To overcome the relatively large adhesive forces, especially for small particles, the centrifuge has to rotate at extremely high speeds. This imposes restrictions on the disk materials that can be used. Based on a stress analysis magnesium was chosen as suitable material.

The rotation also causes a strong gas flow to develop around the disk which creates a force on the particles. These forces were computationally determined and found to be small enough to be neglected; in the simulations the flow force was at most two orders of magnitude smaller than the centrifugal force. The effect of changing particle radius, pressure and rotational speed on the flow force were also analysed and it was found that this did not have a significant negative impact on the relative force magnitude. Rolling of the particle on the disk surface due to gas flow drag will occur. The start of this roll was analytically estimated and it was found that it greatly depends on the particle-surface contact mechanics. Regardless, roll is inevitable when the particle approaches removal.

The centrifuge setup with a magnesium disk is a suitable method of measuring the plasma dust removal force and can withstand the extreme forces. As long as the particles are of large enough size the gas flow force on the particles is negligible compared to the centrifugal force and will not influence the experiment results. Rolling of the particle due to drag force might be a difficulty in measuring the plasma force but the effect can be minimised by using particles with a large contact radius and minimising flow drag.

Contents

1 Introduction

Dust removal is an application of plasma that could be useful in many fields. For example, dust particles are a major problem for Martian rovers [1]. Dust accumulates on the solar panels and thus reduces their ability to collect solar energy. Another example of an application of plasma-based dust removal is the semiconductor industry, where absolute cleanliness of some components is a necessity [1]. Dust interferes with the wafer production.

By exposing a dusty surface to a plasma the dust particles obtain a negative charge and are electromagnetically pulled away from the surface. This force is caused by an electric field generated by the plasma. However, the adhesive forces pulling the particle towards the surface are significant and counteract the removal force. Therefore a different known force is applied to assist the plasma removal force. By changing this known force the exact force the plasma exerts on the particle can be determined. In this experiment a spinning disk which induces a known centrifugal force on the particle is used.

In the next chapter first the forces acting on the particle will be discussed in more detail and it will be explained why using a centrifuge is a practical method of measuring the plasma force. In chapter 2.2 the exact setup will be discussed. Chapter 2.3 concerns an analysis of the substantial internal stresses in the centrifuge and the choice of material. Chapter 3 concerns the effects of the gas flow around the centrifuge and the results of flow simulations to determine the scale of these effects. Firstly an analytical validation of the simulation model is discussed. In chapter 3.2 a 2D model of the disk is analysed, and in chapter 3.3 a 3D model to determine pressure forces on the particle. Lastly in chapter 3.4 rolling of the particle due to flow drag is estimated.

2 Experimental setup and method

2.1 Measurement principle

The forces acting on a dust particle when a plasma is applied can be categorised in adhesive forces and the plasma removal force. These forces pull the particle to and from the surface respectively. The most important adhesive force is the Van der Waals force. The Van der Waals force is a combination of the Keesom, Debye and London interactions and is dominant at small distances. Between an infinitely large surface and a perfect sphere this force is [2, p. 68]

$$F_{VdW} = \frac{Ar_p}{6D^2}, \tag{2.1}$$

where A is the Hamaker constant [3] which is typically 10^{-19} J, r_p is the particle radius (m) and D is the distance between the particle and the surface

(m) as can be seen in figure 1. For a dust particle with a 100 μm radius and a surface separation distance of 0.1 nm, formula 2.1 gives $F_{VdW} \approx 0.2$ mN. However, according to contact mechanics the particle will be slightly deformed. This requires an extra term in the equation to deal with the increased Van der Waals force. To this end Lammers introduces [2, p. 70] a second factor to the equation:

$$F_{VdW} = \frac{Ar_p}{6D^2}(1 + \frac{\alpha^2}{r_p D}), \tag{2.2}$$

where α is the radius of contact (m) between the particle and the surface, see figure 1 as well. The particle radius and the Hamaker constant can be determined rather accurately. However, the separation distance D and the radius of contact α are highly dependent on the surface and particle roughness and vary greatly from particle to particle. A small change in D changes F_{VdW} strongly. This causes the adhesive force to be hard to determine. For example theoretical estimations for a 1 μm particle range from 1 pN [1] according to Flanagan to 1 μN according to Lammers [2].

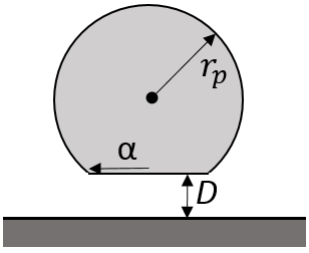

Figure 1: Geometry of a deformed particle on a surface.

Previous experiments have shown that the adhesive force is larger than the plasma removal force, thus the plasma will not cause any particles to be removed from the surface. This means the plasma removal force alone cannot be measured by looking at the release of particles. In order to measure the plasma force exerted on a particle it needs to be assisted with a controllable known force to cause particle removal. This assisting force needs to be exerted on the particle in the same direction as the plasma force, pulling the particle away from the surface. By starting at zero and increasing the known force, the amount of force required for particle release can be determined. When a particle release occurs this means the adhesive forces are slightly smaller compared to the forces pulling the particle away. However when the release force is calculated it is assumed the forces at release are equal. To keep the difference between adhesive forces and removal forces at release as small as possible it is important to ramp up the assisting removal force slowly. A fast increase in assisting force may result in a discrepancy between measured release force and actual release force.

First this procedure is used to determine the combined adhesive force. When the adhesive force has been determined the procedure is repeated for the situation where the plasma is turned on. When a particle is released the adhesive forces are equal to the known force plus the plasma removal force as can be seen in figure 2. The known force should be slightly lower in comparison with the known force needed for removal without plasma. Because the adhesive force has been determined a simple subtraction reveals the plasma removal force.

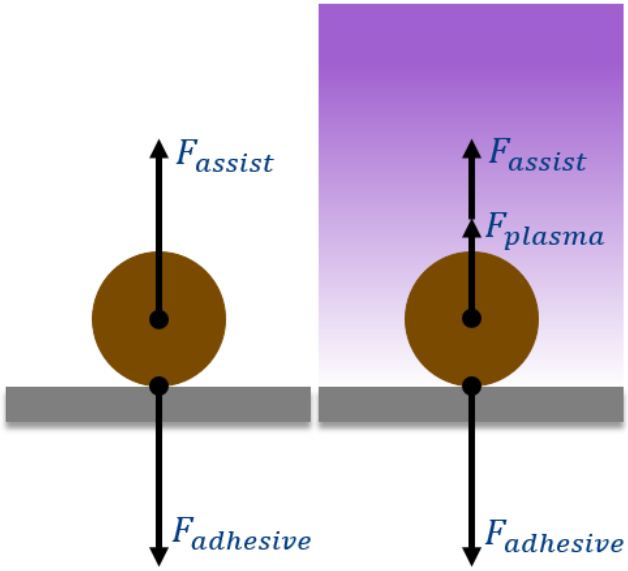

Figure 2: Schematic overview of the forces that act on a particle with and without a plasma present. To the left is the situation without a plasma. At particle release the assisting force must be equal to the adhesive forces. To the right the situation with a plasma can be seen. When a plasma is applied the required assisting force is smaller.

The experimental setup needs to satisfy a couple of requirements. The known force needs to be easily controllable in order to accurately measure the difference between when there is a plasma and when there is not. This means that when measuring the plasma force on very small particles the known force should be very tightly controllable. It should also act in the same direction as the plasma force in order to be able to compare the magnitudes. Ideally the force should be homogeneous across particles on the entire surface and have as few unknown fluctuations as possible. Another requirement is that the known force needs to be able to reach high enough magnitudes to pull particles from the surface, otherwise it would be useless. The last requirement is the ability of the force method to operate in a low-pressure plasma environment.

One setup that satisfies the requirements consists of a vibrating piezo-crystal. Particles on this surface experience an alternating force pulling the particle either from or towards the surface. This setup has been successfully used previously but has a couple of drawbacks. Because of the alternating direction of the force the particle is pushed against the surface each time before it is pulled away. This causes particle deformation. Another drawback is the particle size limitation due to maximum surface acceleration.

2.2 Centrifuge

To overcome the limitations of the vibration setup a new setup was developed consisting of a centrifuge. Spinning a disk with particles on the surface applies a known force to the particles while satisfying all requirements previously mentioned. The rotational velocity of the disk can be changed, applying a known fictitious force of

$$F_{centrifugal} = \frac{mv^2}{r} = m\omega^2 r, \tag{2.3}$$

to the particle where m is the particle mass (kg), v is the particle speed (ms^{-1}) and r is the distance of the particle from the center of rotation (m). The velocity can be expressed in terms of angular velocity ω (rad s^{-1}): $v = \omega r$. The particles used are fluorescent polystyrene particles with a density of 1050 kg m^{-3}.

To be able to create an argon-based plasma at various pressure levels the spinning disk is contained inside a vacuum vessel. This vessel also contains equipment for dispensing dust particles to the surface and monitoring the disk speed. A schematic view of the setup can be seen in figure 3. The axle of the disk is connected to a permanent-magnet motor, Celeroton CM-2-500, not shown in the figure. This motor can be controlled using the CelerotonPilot software on a PC. For removal of small dust particles high rotational speeds are needed. For small particles adhesion force reduces roughly linearly with the radius (formula 2.2), while the centrifugal force 2.3 reduces with the radius to the power three (mass is linear with volume which is cubic). Therefore small particles need high ω for removal. The motor can go up to 500 000 rpm but the vacuum bearing does not support velocities higher than 200 000 rpm. In order to reach 200 000 rpm the disk material needs to be carefully chosen, otherwise it will tear apart. A detailed analysis of the required disk material can be found in chapter 2.3, where ultimately a magnesium disk was chosen based on its properties.

Due to the high energies involved in the spinning of the disk a movable concrete bunker is placed around the vacuum vessel. This bunker consists of approximately 5cm thick tiles surrounding the vacuum vessel completely. A small hole in the top of the bunker provides access for the dust dispenser, which can be lowered and raised from the surface. A hole in the bottom

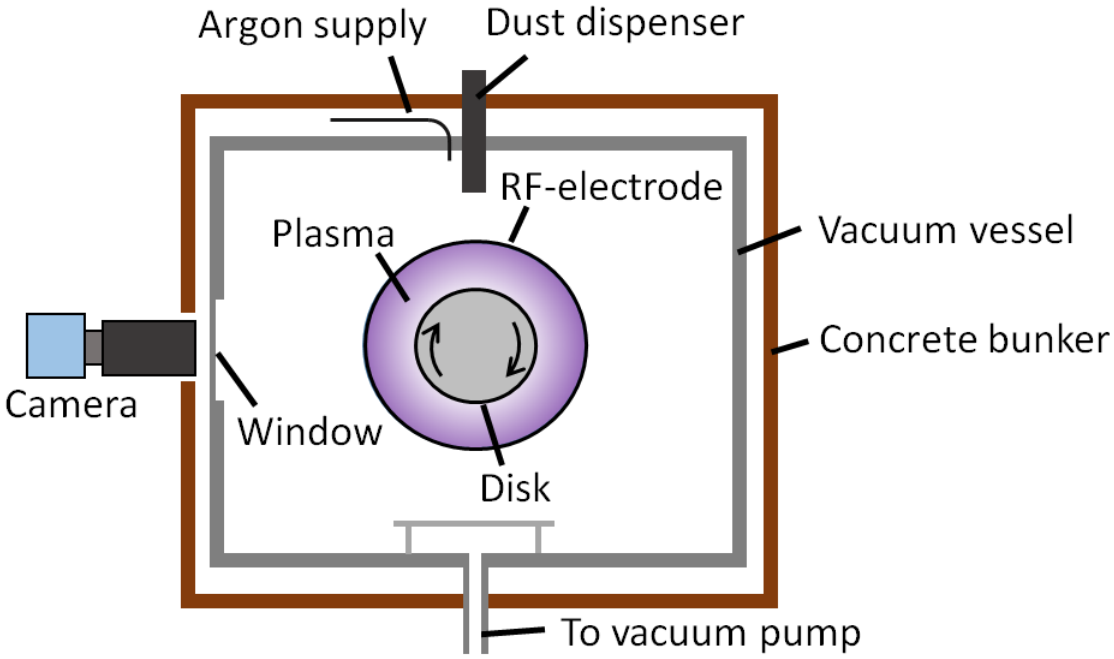

Figure 3: Schematic cross-section of centrifuge setup.

connects the vacuum vessel via valves to the turbo pump, to a large pump, and to open air. The pressure can be set with an automatic control valve.

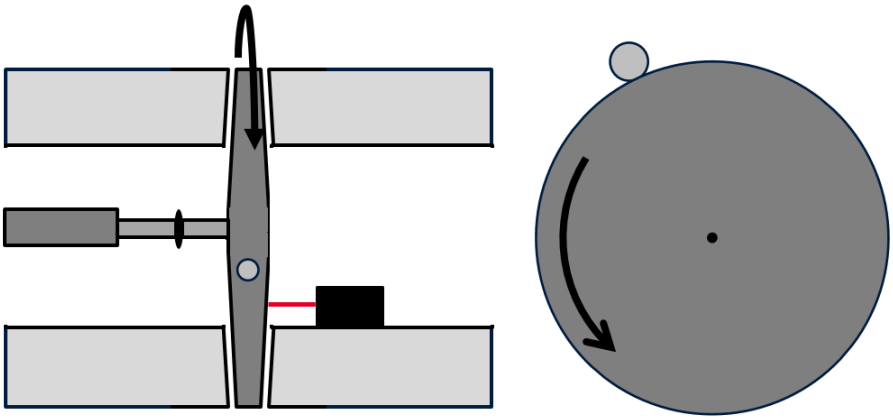

Figure 4: To the left is a schematic cross-section of the disk and motor. The motor is connected with a rubber joint to the disk axle. The particle sits on the outer flat edge of the disk, as seen on the right.

For monitoring the disk a camera is fitted into a hole in the side of the bunker and films the side of the disk. Initially a few spinning particles will be seen by the camera as blurry stripes on the disk which can be counted

when sufficiently spaced out. For higher particle densities the camera will need to be triggered by a sensor at exactly the right moment to ensure the same side of the disk is captured with each frame. This proximity sensor will be mounted next to the large flat side of the disk (see figure 4) and measures a different signal depending on which half of the disk is passing along. By counting these passes the system can determine when the right time is for another camera capture as well as determine the exact rotational speed of the disk. The C++ code for this system can be found in appendix 6.1. The measured speed can differ from the speed provided by the motor because the axle to the motor is connected by a rubber joint which can slip for safety reasons. Slippage will result in different speeds. However, when slippage occurs the rubber connection is likely to be destroyed altogether and the disk will immediately start to stop spinning. At low velocities (sub 1000 rpm) the motor is not able to measure the speed. Therefore it is important mostly in the low velocity region to have this secondary method of getting the disk velocity. A laser (or bright lamp) next to a window panel on the side of the vessel will provide a light spot on the disk to improve the brightness of camera frames captured at high speeds where low shutter times are needed.

2.3 Internal disk stress

The internal disk forces are substantial and need to be taken into account when choosing the disk material. Determining internal stress in disks is a recurring problem in engineering, for example in the design of turbines and flywheels. Stress induced by rotation is axisymmetrical about the axis of rotation. The cause of the internal stress is the centrifugal force. This force can be expressed per unit volume as

$$F_{centrifugal} = \rho r \omega^2, \tag{2.4}$$

acting in the radial direction. Here ρ is the material density (kg m^{-3}), r is the radius (m) and ω is the angular velocity (rad s^{-1}). The stress induced by this force has a radial and a tangential component, σ_r and σ_θ (N m^{-2}). The stress components are according to Ragab and Bayoumi [4, eq. 4.37]

$$\sigma_r = \frac{A}{r^2} + 2C - \frac{3+\nu}{8}\rho\omega^2 r^2, \tag{2.5a}$$

$$\sigma_\theta = -\frac{A}{r^2} + 2C - \frac{1+\nu}{8}\rho\omega^2 r^2, \tag{2.5b}$$

for axisymmetrical problems where A and C are constants and ν is Poisson's ratio, a material constant. When a material is stretched it usually compresses in the directions perpendicular to the direction of the stretch. Poisson's ratio is the fraction of expansion divided by the fraction of compression.

At the center of the disk there is no difference between the radial and tangential stress component. Therefore $\sigma_r(0) = \sigma_\theta(0)$. From this can be deduced that the constant A in 2.5 must be zero. The constant C can be determined with the boundary condition $\sigma_r(R) = 0$, where R is the disk radius (m). This implies that there is no internal stress in the radial direction at the edge of the disk. Applying the boundary condition to 2.5a gives

$$C = \frac{1}{16}(3+\nu)\rho\omega^2 R^2. \tag{2.6}$$

Substituting this expression for C into 2.5 gives the final stress components:

$$\sigma_r = \frac{3+\nu}{8}\rho\omega^2(R^2 - r^2), \tag{2.7a}$$

$$\sigma_\theta = \frac{3+\nu}{8}\rho\omega^2(R^2 - \frac{1+3\nu}{3+\nu}r^2). \tag{2.7b}$$

The relative magnitude of the components have been plotted in figure 5. At the center the stresses are equal but along the radius of the disk the radial stress component decreases faster than the tangential component. At the edge of the disk radial stress has disappeared and only tangential stress is present.

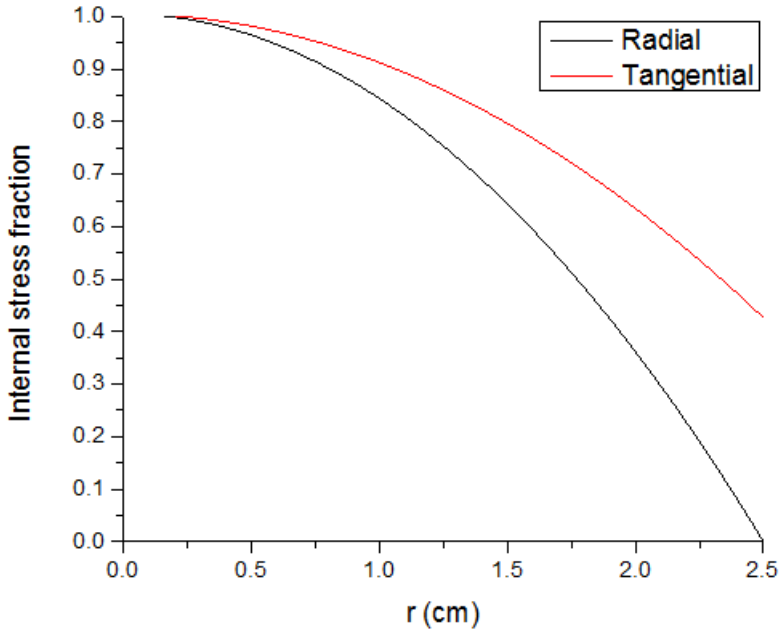

Figure 5: Relative internal stress components in a constant-width disk with a 2.5 cm radius.

The maximum internal stress for a constant-width spinning disk occurs

at $r = 0$:

$$(\sigma_r)_{max} = (\sigma_\theta)_{max} = \frac{3+\nu}{8}\rho\omega^2 R^2. \tag{2.8}$$

The maximum rotational velocity was calculated for a few materials and can be found in table 1. The material used in the setup needs to have a theoretical maximum rotational velocity beyond 200 000 rpm as well as be light enough for the bearings. Industrial diamond has an extremely high theoretical maximum angular velocity but is too heavy (estimated mass of 48 grams). A constant-width titanium disk could also be utilised, but like the diamond a titanium disk is too heavy for the motor (estimated 43 grams). Magnesium however is not as heavy and provides good ultimate tensile strength. The maximum velocity will be even higher for a conical shaped disk. This makes magnesium the material of choice for the disk.

Table 1: Various disk materials and their theoretical maximum angular velocity on a 2.5 cm disk. S is the material's ultimate tensile strength.

Name	ρ (kg m^{-3})	ν	S (MPa)	Constant width (rpm x1000)
Steel, high strength alloy	7800	0.305	760	186
Structural steel	7800	0.303	475	147
Magnesium	1740	0.35	285	239
Copper	8920	0.355	220	93
Aluminium	2700	0.334	300	197
Tungsten	19250	0.28	1510	167
Diamond	3500	0.2	2800	540
Titanium (grade 5 alloy)	4420	0.342	950	274

The previous stress analysis shows an unfavourable stress distribution where the largest stress occurs at the center of the disk. In order to improve this distribution an increase in disk thickness at the center can be used, with reducing thickness towards the edge of the disk. A disk with linearly reducing thickness is called a conical disk. The thickness reduces from the maximum at the center to 0 at $r = R$, the edge of the disk. A disk with a flat outer edge has an apparent radius R' smaller than its real radius R as can be seen in figure 6.

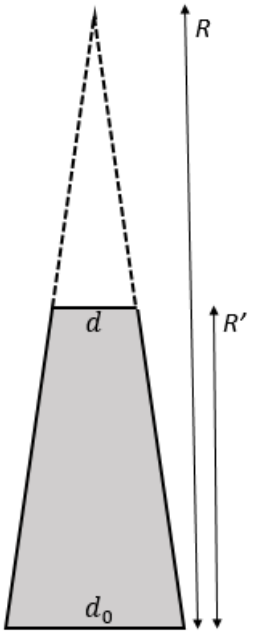

Figure 6: Schematic cross section of a conical disk with linearly reducing thickness.

The ratio of d_0 to d enhances the disk strength. When d_0 is larger than d this decreases the maximum stress in the disk, thus increasing the maximum rotational velocity the disk can handle without tearing apart. The disk used in the experiment will have a thickness ratio of 2:1.

3 Gas flow analysis

The main consequence of the gas flow around the disk is its effect on particles on the disk. The velocity of the particle is higher than that of the gas flow so a pressure field will develop around the particle, pushing the particle in the counter-direction of rotation. If this tangential force is strong enough it could sweep the particle from the disk surface. The pressure field will also cause a vertical force, either pushing the particle towards or pulling it from the surface. These forces can be determined by integration of the pressure field over the particle surface. However, the pressure field is not easily determined. That is why simulations are used. First the simulation software is validated by comparing the result of a similar model to an analytic solution. Next a simple model of only the disk will be discussed and finally a full model of both the disk and the particle.

3.1 Analytical validation

First the flow between two concentric circular cylinders of infinite length is determined analytically. Here cylindrical coordinates are used. The inner cylinder has a radius R_1 and the outer a radius of R_2 as can be seen in figure 7. The three-dimensional cylindrical Navier-Stokes equations are defined as follows [6]

$$\rho(\frac{\partial v_r}{\partial t} + v_r\frac{\partial v_r}{\partial r} + \frac{v_\theta}{r}\frac{\partial v_r}{\partial \theta} - \frac{v_\theta^2}{r} + v_z\frac{\partial v_r}{\partial z}) = \\ -\frac{\partial P}{\partial r} + \rho g_r + \mu(\frac{\partial}{\partial r}(\frac{1}{r}\frac{\partial}{\partial r}(rv_r)) + \frac{1}{r^2}\frac{\partial^2 v_r}{\partial \theta^2} - \frac{2}{r^2}\frac{\partial v_\theta}{\partial \theta} + \frac{\partial^2 v_r}{\partial z^2}), \quad (3.1a)$$

$$\rho(\frac{\partial v_\theta}{\partial t} + v_r\frac{\partial v_\theta}{\partial r} + \frac{v_\theta}{r}\frac{\partial v_\theta}{\partial \theta} + \frac{v_r v_\theta}{r} + v_z\frac{\partial v_\theta}{\partial z}) = \\ -\frac{1}{r}\frac{\partial P}{\partial \theta} + \rho g_\theta + \mu(\frac{\partial}{\partial r}(\frac{1}{r}\frac{\partial}{\partial r}(rv_\theta)) + \frac{1}{r^2}\frac{\partial^2 v_\theta}{\partial \theta^2} + \frac{2}{r^2}\frac{\partial v_r}{\partial \theta} + \frac{\partial^2 v_\theta}{\partial z^2}), \quad (3.1b)$$

$$\rho(\frac{\partial v_z}{\partial t} + v_r\frac{\partial v_z}{\partial r} + \frac{v_\theta}{r}\frac{\partial v_z}{\partial \theta} + v_z\frac{\partial v_z}{\partial z}) = \\ -\frac{\partial P}{\partial z} + \rho g_z + \mu(\frac{1}{r}\frac{\partial}{\partial r}(r\frac{\partial v_z}{\partial r}) + \frac{1}{r^2}\frac{\partial^2 v_z}{\partial \theta^2} + \frac{\partial^2 v_z}{\partial z^2}). \quad (3.1c)$$

The inner cylinder rotates with an angular velocity ω along the center axis, the outer one is static. Since the system is rotationally symmetric, infinitely long and in a steady state no parameter should be a function of θ, z and t respectively:

$$\frac{\partial}{\partial \theta} = \frac{\partial}{\partial z} = \frac{\partial}{\partial t} = 0. \quad (3.2)$$

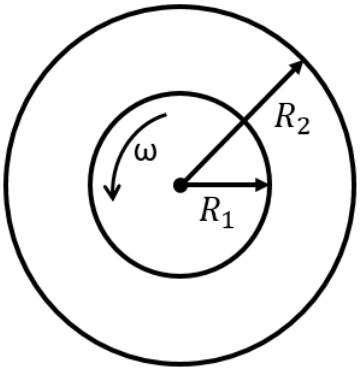

Figure 7: Two infinitely long concentric cylinders.

The flow is assumed to be circular meaning the velocity vector cannot contain a z or r component:

$$v_z = v_r = 0. \tag{3.3}$$

The rotationally symmetric flow implies gravity can be neglected. With the simplifications and assumptions 3.1 reduces to:

$$-\rho\frac{v_\theta^2}{r} = -\frac{\partial P}{\partial r}, \tag{3.4a}$$

$$0 = \mu\frac{\partial}{\partial r}(\frac{1}{r}\frac{\partial}{\partial r}(rv_\theta)), \tag{3.4b}$$

$$0 = -\frac{\partial P}{\partial z}. \tag{3.4c}$$

3.4a provides the radial pressure distribution due to centrifugal forces. Because v_θ is only a function of r equation 3.4b can be converted from partial differential to an ordinary differential equation:

$$\frac{\mu}{r}\frac{d}{dr}(rv_\theta) = C_1, \tag{3.5}$$

where C_1 is a constant. Integration gives an expression for v_θ:

$$v_\theta = C_1\frac{r}{2\mu} + \frac{C_2}{r}, \tag{3.6}$$

where C_2 is also a constant. The constants can be found using boundary conditions. The first boundary condition is the no-slip condition on the inner wall: $v_\theta = \omega R_1$ at $r = R_1$. The second is the no-slip condition on the outer wall: $v_\theta = 0$ at $r = R_2$. Applying the second boundary condition to 3.6 provides an expression for C_2:

$$0 = C_1\frac{R_2}{2\mu} + \frac{C_2}{R_2} \rightarrow C_2 = -\frac{C_1R_2^2}{2\mu}. \tag{3.7}$$

Applying the first boundary condition to 3.6 and substituting C_2 with 3.7 provides an expression for C_1:

$$\omega R_1 = C_1 \frac{R_1}{2\mu} - \frac{C_1 R_2^2}{2\mu R_1} \rightarrow C_1 = -\frac{2\mu\omega R_1^2}{R_2^2 - R_1^2}. \tag{3.8}$$

Using these expressions for C_1 and C_2 and substituting them in the original expression for v_θ gives:

$$v_\theta = -\frac{2\mu\omega R_1^2}{R_2^2 - R_1^2}\frac{r}{2\mu} + \frac{\omega R_1^2 R_2^2}{r(R_2^2 - R_1^2)} \rightarrow v_\theta = \frac{\omega R_1^2}{R_2^2 - R_1^2}\left(\frac{R_2^2}{r} - r\right). \tag{3.9}$$

This analytic solution is used to verify the flow simulation software, in this case COMSOL Multiphysics is used [7]. The 2D axisymmetric model consists of a rectangle with the left side at $r = 2.5$ cm and the right side at $r =$ 5cm. The top and bottom are connected to form a flow continuity pair. This means the model can be stacked and is effectively infinitely long. The rotational velocity ω is 200 000 rpm, like the disk in the setup. Applying the boundary conditions and solving the model for a stationary solution results in a velocity profile that is highly similar to the analytic solution, as can be seen in figure 8, with a maximum relative difference of $3.81 * 10^{-4}$.

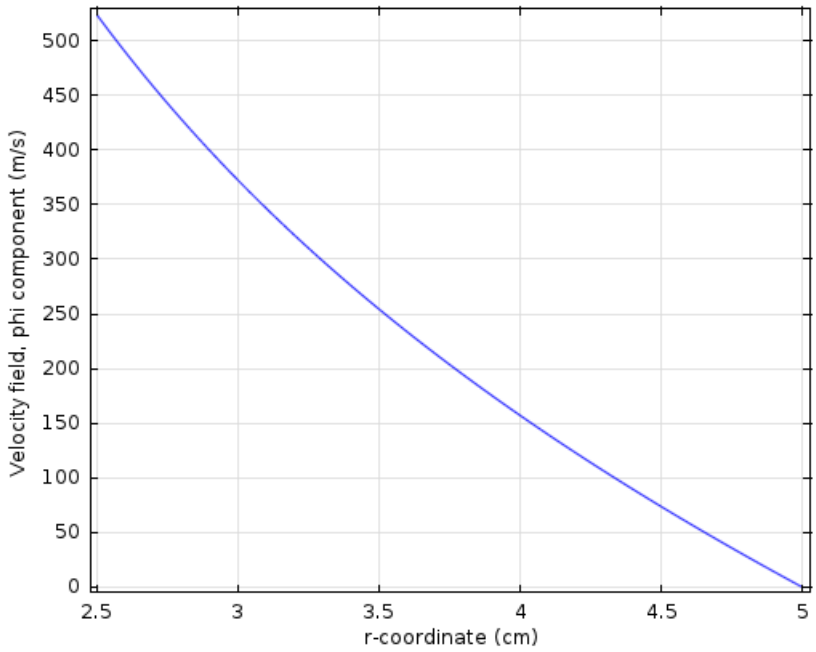

Figure 8: Tangential flow velocity between two concentric cylinders, overlapping analytic and simulation result.

3.2 Model of the disk

In order to better simulate the disk used in the experiment the width of the disk needs to be taken into account. For this a 2D axisymmetric model is used similar to the analytic comparison model, but it's not infinitely long and just a small part of the inner cylinder is rotating. Between the rotating disk and the grounded cylindrical electrode next to it there is a small gap (see figure 4). The flow in this gap is very complicated due to the vicinity of two surfaces with a large difference in rotational velocity. The Knudsen number is useful for determining the best flow simulation method:

$$Kn = \frac{\lambda}{L}, \tag{3.10}$$

where λ is the particle mean free path (m) and L is a characteristic physical length scale (m). The Knudsen number is mainly used for determining whether continuum or statistical fluid simulation needs to be used. When Kn is larger than approximately 0.1 the particle mean free path relatively large in comparison with the characteristic length scale of the flow and the continuum fluid simulation is not a good approximation any more. This greatly increases the simulation complexity. The width of the gap between the disk and the cylinder is approximately 0.5 mm. This is the characteristic length scale for the flow between the surfaces. The mean free path for particles with a Maxwell velocity distribution is according to S. Chapman and T.G. Cowling [8]

$$\lambda = \frac{1}{\sqrt{2}n\sigma}, \tag{3.11}$$

where the particle density $n = p/k_bT$ (m^{-3}) with p the pressure (Pa) k_b Boltzmann's constant (JK^{-1}) and T the temperature (K), and the 'effective' particle cross-section $\sigma = \pi d^2$ (m^2) with d the particle diameter (m). To calculate the mean free path for argon gas in the centrifuge room temperature (293.15 K), medium vacuum pressure (100 Pa) and the diameter of an argon particle (0.4nm) are used. With 3.11 a mean free path of $\lambda = 5.7 * 10^{-5}$ m is found. The Knudsen number for the flow in the gap is $Kn = 0.11$, which means a statistical fluid simulation should be used. Most flow simulation programs cannot solve this accurately. Therefore the small gap is neglected and replaced by a slip region on the cylinder.

The entire simulation domain can be seen in figure 9. The domain is axisymmetric about the z-axis. The left side of the domain is split into three sections. The top section labelled 1 represents the edge of the disk and has a no-slip condition where the ϕ-component of the velocity is set to ωr, where ω (rad s^{-1}) is the disk angular velocity. Section 2 represents the gap between the disk and the cylinder, as described previously, and is given a slip boundary condition. Section 3 is the metal cylinder next to the disk and section 4 the edge of the large disk for structural integrity. Section 5 is

the surface of the casing around the cylinder. Sections 3, 4 and 5 represent static surfaces. These are given a no-slip condition with a velocity of zero. The surfaces represented by section 4 and 5 contain some holes which are not taken into account. Finally section 6 is a symmetric boundary. The simulated domain represents the bottom half of the real system. This is done in order to reduce computing cost and speed up the simulation. The no-slip boundary conditions cause shear stress of the fluid on the surface which will need to be taken into account. The shear stress τ (Nm^{-2}) is given by:

$$\tau(y) = \mu \frac{\partial u}{\partial y}, \tag{3.12}$$

where y is the height above the no-slip surface (m), u is the gas velocity along the surface (ms^{-1}) and μ is the dynamic viscosity of the gas (Pa s).

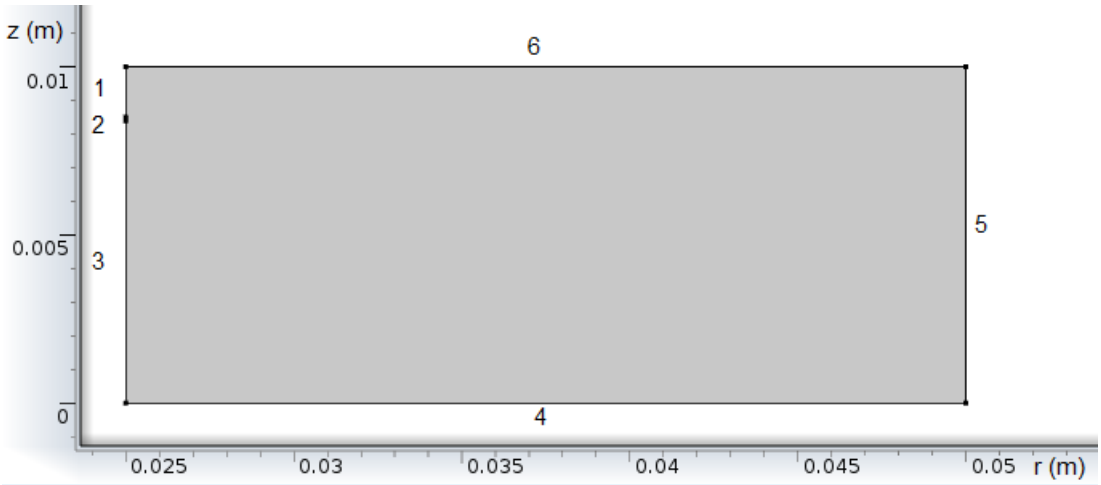

Figure 9: 2D axisymmetric model used in disk flow simulations without any particles present.

The initial conditions of the system are chosen as close to the values used in the real experiment as possible. The pressure is set to 100 Pa and the rotational velocity of the disk is set to match 200 000 rpm, the highest rotational velocity that will be used in the experiment. Finally the material properties are set to match argon gas.

The result of this simulation can be seen in figures 10 and 11, showing the ϕ-component of the velocity and the velocity magnitude on a slice of the domain respectively. From these results can be seen that the 'swirl' flow (ϕ component) has a greater velocity than the plane flow (r and z components). This is expected because the spinning disk causes high gas flow velocities at the surface. Flow in the radial plane is only caused by centrifugal force acting on the gas when it is being rotated by the disk. As can be seen with the plane flow streamlines in figure 11 this will propel the gas outward,

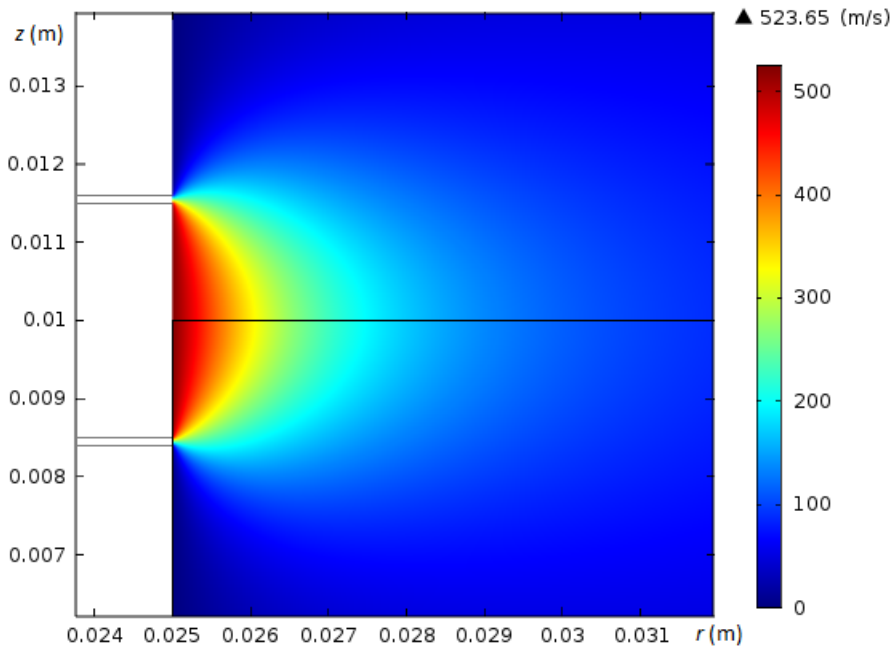

Figure 10: Velocity ϕ-component of the 2D simulation at 200 000 rpm in argon gas. Due to cylindrical symmetry this swirl velocity profile is independent of direction of rotation.

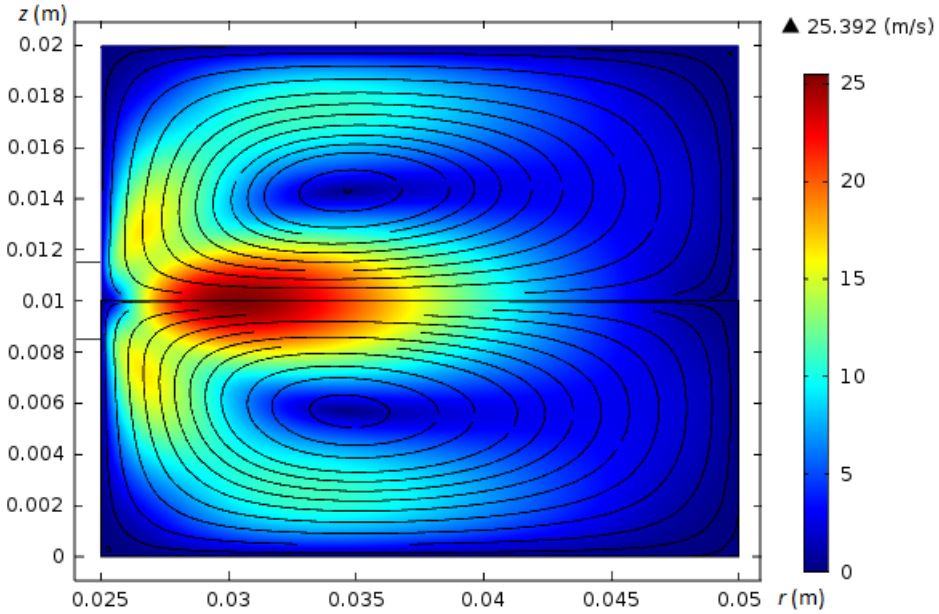

Figure 11: Plane flow streamlines and velocity magnitude in a slice of the domain.

away from the disk, until it encounters the outer edge of the domain. At that point the gas will flow away from the middle ($z = 0.01$ m) and back along the top and bottom edges.

Due to replacing the gap with a small slip-flow surface the simulation results are likely not entirely correct, especially near this gap. However overall it provides a good approximation of how the gas will flow around the disk. The main point of interest for the experiment is the flow around a particle on the surface. This will be discussed in the next chapter.

3.3 Model of the particle

As can be seen in figure 10 the ϕ-component of the flow velocity quickly drops off away from the disk. However the velocity of a point attached to the disk such as on an attached particle increases linearly with radius ($v = \omega r$). This causes any protrusion on the disk to move faster than the gas flow. The larger the protrusion the larger the velocity difference will be. This difference causes a particle on the surface to experience a drag force. The nature of the flow around the particle can be predicted by determining the Reynolds number [9]:

$$Re = \frac{\rho L v}{\mu}, \tag{3.13}$$

where v is the mean velocity of the particle relative to the fluid (ms^{-1}), L is the characteristic length scale (m), in this case the particle diameter, ρ is the gas density (kg m^{-3}) and μ is the dynamic viscosity of the gas (Pa s). Reynolds numbers in the low region (<10) indicate a pure laminar flow which is characterised by smooth, fluid motion. Higher Reynold flows change into turbulent flows which creates chaotic instabilities.

Using equation 3.13 and the flow velocity profile acquired in the 2D simulations the Reynolds number can be estimated for flow around dust particles on the surface. The mean relative velocity is chosen as the relative velocity at the center of the particle. As can be seen in figure 12 the relative velocity is 0 at the edge of the disk and increases quickly. Choosing the mean relative velocity at the center of the particle is an approximation because the increase in relative velocity is not linear. However, for very small particles this linear approximation does not have a large impact. The characteristic length is $2r_p$, where r_p is the particle radius (m). This gives an expression for the particle Reynolds number:

$$Re_p = \frac{\rho 2 r_p}{\mu}(\omega r - v_{flow,\phi}). \tag{3.14}$$

Calculating equation 3.14 for various particle radii shows an increase in Reynolds number for larger particles as can be seen in figure 13. This is expected because the characteristic length scale L increases as well as the relative velocity.

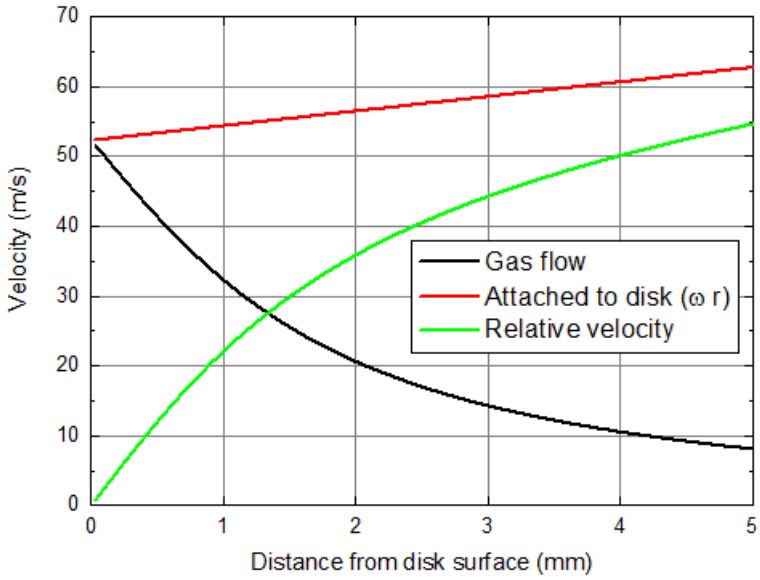

Figure 12: Velocity comparison of a point attached to the disk and the gas flow.

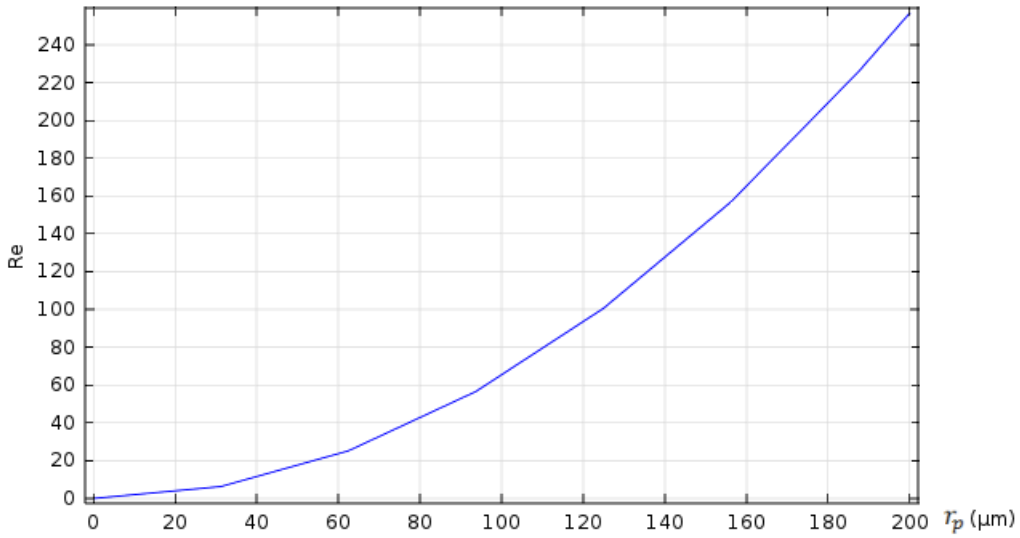

Figure 13: Estimated Reynolds number as function of particle radius.

Particles used in the experiment have a maximum radius of 50 µm. The results show the Reynolds number for these sizes should stay below the value of 20. Flow around particles with radius <35 µm have a Reynolds number of roughly 10 or lower and should be purely laminar. Because the Reynolds number stays relatively low the simulations can be done without including a

turbulence model. This improves simulation speed and should maintaining accuracy.

The modelling of the particle is not possible in the 2D axisymmetric model. This is because if a circle were added on the inner boundary it would result in a tube along the edge of the disk due to the axisymmetry. Therefore a 3D model has to be used consisting of the entire domain volume around the disk and the particle. This model is equal to the 2D axisymmetric model if it were revolved around the z-axis. To verify this transition from a 2D model to a 3D one the velocity profile generated by the 3D model using the same settings is compared against the profile generated by the 2D model. Because these profiles were equal to each other it can be assumed that the models are consistent. A sphere of variable radius is added to the inner edge of the 3D domain to represent a particle. The particle is located exactly in the middle of the disk at $z = 1$ cm. At this point the flow velocity reaches the highest value. The entire simulation volume is (taking symmetry into account) 2 cm high. This height was determined by doing multiple simulations with different volume heights and comparing the results. To optimise computation time the smallest height was chosen without a change in result.

There is one major difference in the 2D and 3D simulation models. In the 2D model the disk is given a boundary condition of $v_\theta = \omega r$. This boundary condition makes the disk surface act like a conveyor belt, which is identical to if the disk were actually spinning. However a problem arises when a particle is added. In contrary to the disk the particle actually changes position. Modelling this changing geometry increases computation time and is not convenient. Because the particle is the only object in the simulation changing position a better solution for the simulation would be to change the reference frame to that of the particle. This involves keeping the particle (and consequently the disk) static and applying the rotational condition to the non-rotating parts of the system which are the gas (initially) and the edges of the domain. However when one changes to a rotating frame of reference one needs to take into account the fictitious forces that arise. These forces are the centrifugal force, the Coriolis force and the Euler force:

$$F_{centrifugal} = -m\boldsymbol{\Omega} \times (\boldsymbol{\Omega} \times \boldsymbol{r}), \tag{3.15a}$$

$$F_{coriolis} = -2m\boldsymbol{\Omega} \times \boldsymbol{v}, \tag{3.15b}$$

$$F_{euler} = -m\frac{d\boldsymbol{\Omega}}{dt} \times \boldsymbol{r}, \tag{3.15c}$$

where m is the mass of a body (kg), $\boldsymbol{\Omega} = \begin{pmatrix} 0 \\ 0 \\ \omega \end{pmatrix}$ is the angular velocity

vector, $\boldsymbol{v} = \begin{pmatrix} u \\ v \\ w \end{pmatrix}$ the body velocity vector and $\boldsymbol{r} = \begin{pmatrix} x \\ y \\ z \end{pmatrix}$ the body position vector. In the model the only rotation is about the z-axis: $\boldsymbol{\Omega} = \omega \boldsymbol{z}$. The Euler force is only applicable in case of a time-dependent rotating reference frame, which is not the case in these simulations. Because the fictitious forces act on the entire gas volume the equations of 3.15 can be most conveniently implemented as a body force vector $\boldsymbol{f}$ (Nm^{-3}):

$$\boldsymbol{f} = \rho\omega^2 \begin{pmatrix} x \\ y \\ 0 \end{pmatrix} - 2\rho\omega \begin{pmatrix} -v \\ u \\ 0 \end{pmatrix}. \tag{3.16}$$

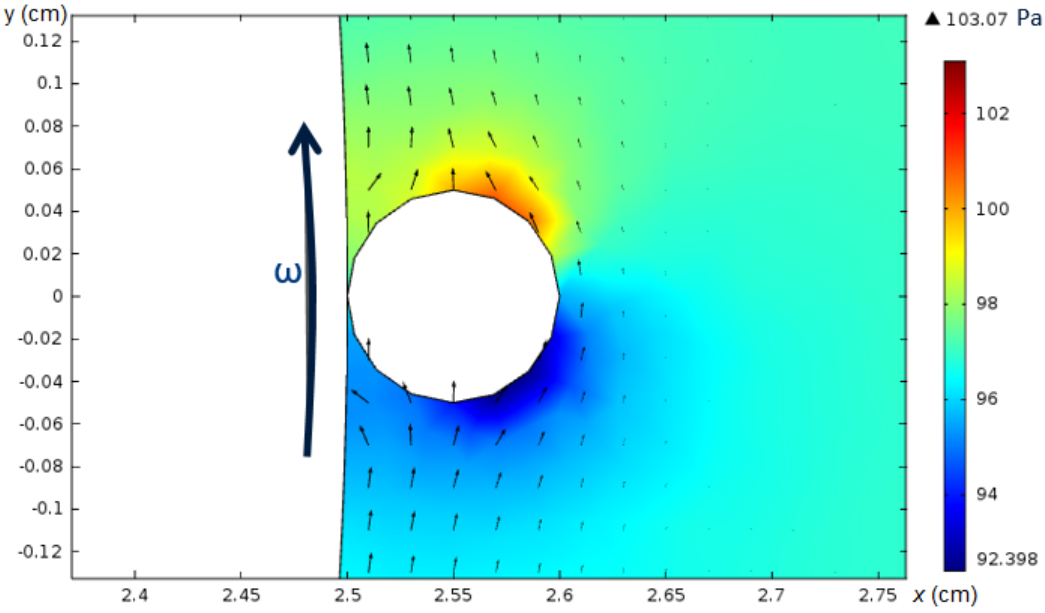

Figure 14: Gas pressure and velocity field around the particle on the $z = 1$ cm plane.

An example result of a simulation can be seen in figure 14, using typical values of 20 000 rpm at 100 Pa but an exaggerated particle diameter of 1 mm. This figure shows the pressure field that develops around the particle on the $z = 1$ cm plane. In the figure the disk along with the particle is rotating counterclockwise as indicated by the large arrow. This rotation causes a flow to develop in the same rotational direction. However, the flow velocity quickly drops away from the disk as was discussed previously and can be seen in figure 12. The increase in relative velocity causes an increase in pressure in front of the particle, where gas is pushed away, and a decrease behind the particle, in the wake of the particle movement. The force exerted

on the particle by the gas is determined by integrating the pressure and shear stress over the surface. This force can be split into a tangential component $F_{tangential}$ and a radial component F_{radial}. There is also a force component in the z-direction but this component is zero due to the positioning of the particle on the $z = 1$ cm symmetry plane.

Ideally the flow force should be much smaller than the centrifugal force. If it were of the same or higher order it would need to be taken into account when determining the plasma force. This is because the presence of a plasma force lowers the rotational velocity needed for particle release and this will consequently lower the force of gas flow on the particle. To compare the order of magnitude of flow force on the particle to that of centrifugal force both forces have been calculated from the simulations and can be seen in figure 15. For the centrifugal force calculation a particle density of 1050 kg m^{-3} was used, equal to that of the fluorescent polystyrene particles. The smallest particle radius that was modelled is 50 µm. Smaller radii were attempted but at that point the model geometry became too small for the simulation software to handle.

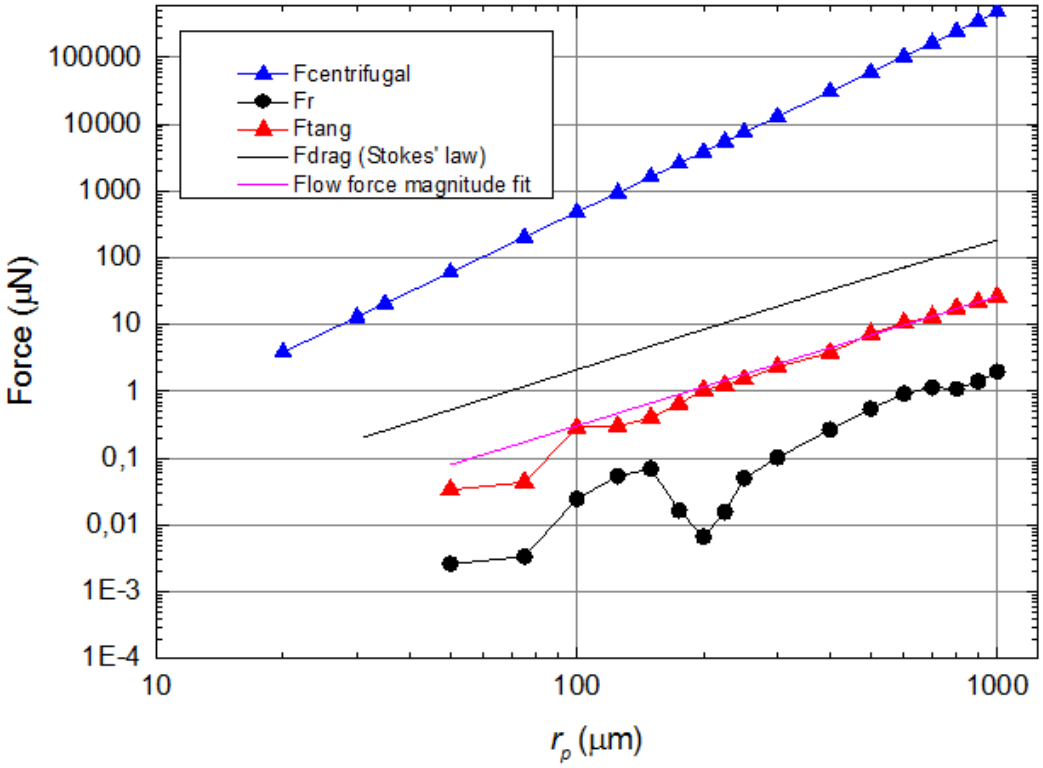

Figure 15: Particle force order of magnitude comparison as function of particle radius at 20 000 rpm and 100 Pa. A fit based on equation 3.18 is made with the flow force magnitude.

In the figure can be seen that for all computations with different particle radii the tangential component is larger than the radial force component. The difference ranges from more than two orders of magnitude to less than one. This is expected because the main pressure gradient is in the tangential direction as can be seen in figure 14. Both the tangential and radial force components generally decrease as the radius decreases. There are a few irregularities in the decrease of force, most notably the radial flow force at $r_p \approx 200$ µm, but these could be due to computational issues. The overall decrease has two causes. Firstly the surface area A_p of particle decreases with the radius of the particle squared ($A_p = 4\pi r_p^2$), causing a smaller force after surface pressure and shear stress integration. Secondly the smaller a particle is the smaller the velocity difference with the gas flow. A smaller velocity difference causes a smaller pressure gradient to develop around the particle and thus causes a lower flow force. If the force follows both the quadratic reduction in surface area and the linear reduction in relative velocity it should decrease with $F_{flow} \sim r_p^3$.

The drag force exerted on a free spherical object at low Reynolds numbers can be expressed with Stokes' law:

$$F_{drag} = 6\pi\mu r_p v, \tag{3.17}$$

where μ is the dynamic viscosity (Pa s) and v the relative flow velocity (ms^{-1}). According to this equation and assuming that for small particles the relative velocity increases linearly (see figure 12) the drag force should increase in a quadratic fashion with particle size $F_d \sim r_p^2$. However Stokes' law only applies in case of a particle being hit by a uniform flow. The actual particle is next to a relatively large surface and thus in a non-uniform flow. For comparison the Stokes' drag force has been plotted in figure 15. The slope is similar to the slope of the computed flow forces, which will be calculated later.

For all radii in the range of 50 to 1000 µm the flow force magnitude is smaller than the centrifugal force magnitude. At most (at $r_p = 50$ µm) the relative magnitude is 0.0006 compared to the centrifugal force, which is small enough to be neglected when calculating the plasma force. In the figure it can be seen that the relative magnitude increases as the radius decreases. The results can be extrapolated to determine the radius at which the flow force is not negligible any more. For this the flow force magnitude ($\sqrt{F_{tang}^2 + F_r^2}$) is fitted to a line in the logarithmic plot parametrised by

$$F_{fit} = A r_p^B, \tag{3.18}$$

where F_{fit} is the force in µN, r_p is of the unit µm, A is a constant with the appropriate unit (depending on the value of B) and B is a dimensionless constant. The result of the fit can be found in table 2 and is visualised

in figure 15. From the result can be deduced that the flow force scales with particle size as roughly $F_{flow} \sim r_p^{1.94}$. This is a smaller slope than the cubic dependency on radius predicted with just the surface area and relative velocity equations. However that prediction does not take any flow effects into account and is extremely basic. This is more similar to the quadratic dependency found with Stokes' law. The drag force calculated with Stokes' law is generally at least an order of magnitude larger. This could be because Stokes's law is for free particles in an uniform flow, which is not the case here.

Using the fit results a simple equation can be solved to estimate the radius $r_{critical}$ at which the flow force magnitude is more than one tenth of the centrifugal force. It is found that this occurs at $r_{critical} \approx 0.84$ µm. However, it is not certain the fit for the flow force magnitude is correct for radii smaller than those modelled. The particles used in the experiment will have a radius not smaller than 10 µm so $r_{critical}$ is not a concern.

Table 2: Result parameters of the fit for the flow force magnitude as function of particle radius using equation 3.18.

	Value	Uncertainty
A	4.0e-5	1.0e-5
B	1.941	0.036

The change of flow force on the particle when the pressure parameter is changed has also been modelled and analysed at typical values of 20 000 rpm and $r_p = 50$ µm. The result of these computations can be seen in figure 16. For these computations the shear stress force on the particle was not taken into account. This means the actual flow forces acting on the particle are larger than the ones computed in these results. However, from previous results it is known that the shear flow force is roughly equal to the force due to the pressure field. The difference between the centrifugal force and the flow forces is the orders of magnitude which means the flow force found in these results is representative of the actual force with shear flow taken into account.

In the results one can see that the centrifugal force is not dependent on the gas pressure and remains constant. As expected a decrease in pressure also decreases the force of gas flow on the particle, since less gas molecules will impact with the particle. By extrapolating the gas force one can speculate that the force will become relatively large compared to the centrifugal force at very high pressures. However for this experiment this is not a concern since these high pressures will not be used. These high pressures do present a method of experimentally measuring the flow force. By changing the pressure and determining the centrifugal force needed for release with high and low pressures the change could be noticed if it is large enough. For

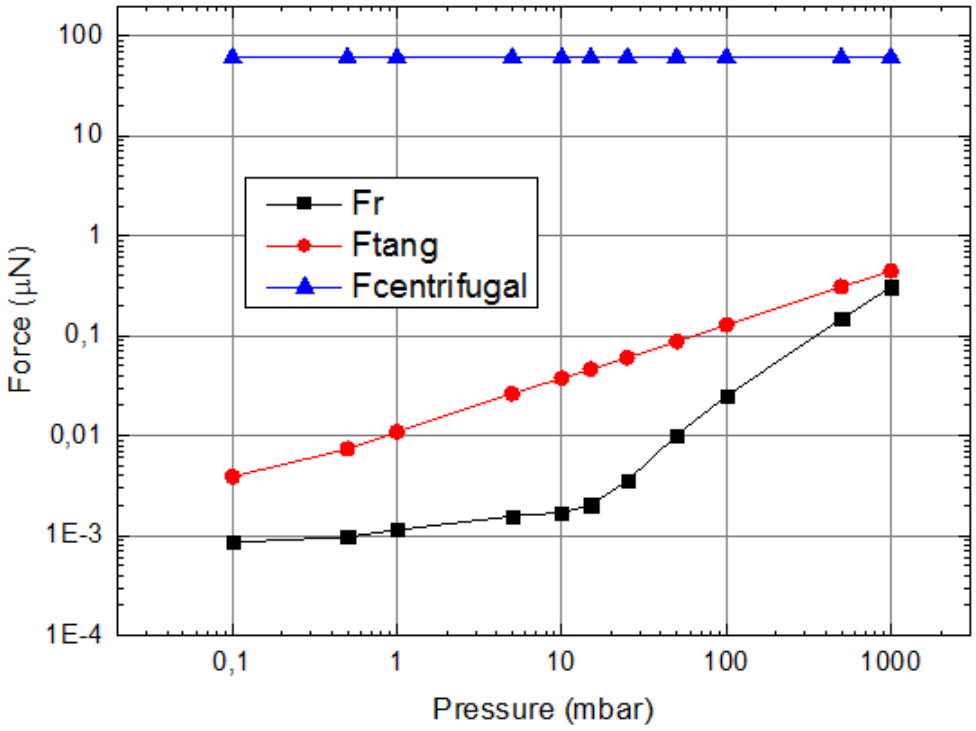

Figure 16: Particle force order of magnitude comparison as function of gas pressure at 20 000 rpm and $r_p = 50$ µm. Shear flow stress on the particle is not taken into account, which means the flow force values are roughly a factor 2 too low.

this high pressures would need to be used, otherwise the change is too small to make a difference in the required centrifugal force.

Finally the gas flow force for different rotational velocities is computed, see figure 17. The flow force has also been calculated without taking shear stress force into account. Computations with speeds higher than 30 000 rpm were attempted, up to 200 000 rpm, but unsuccessful. Computational difficulty increases for high velocities because the flow approaches and passes Mach 1. This happens at roughly 125 000 rpm. For the rotational velocities that were modelled the change in rpm did not result in a particularly large change in relative force magnitude. If this is similar for other particle size and gas pressure values changing the disk velocity should not negatively impact the relative force magnitude.

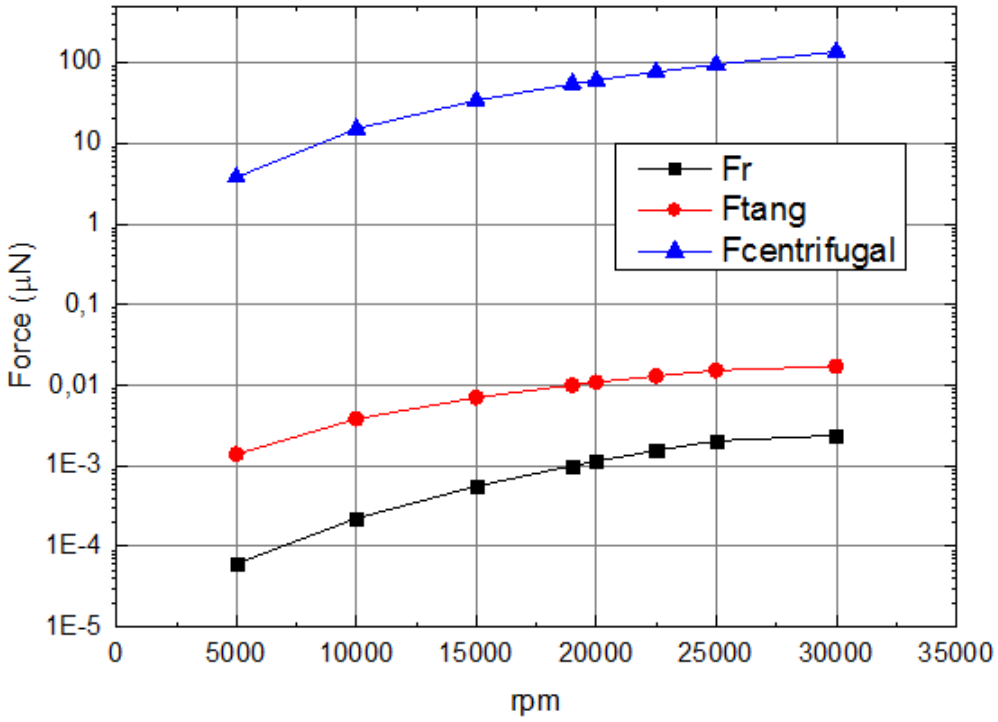

Figure 17: Particle force order of magnitude comparison as function of disk rotational velocity at 100 Pa and $r_p = 50$ µm. Shear stress not taken into account.

3.4 Flow induced particle torque

The only force to have a non-radial component is the flow force, which has a tangential component as described in chapter 3.3. The forces acting on the particle result in a torque vector $\boldsymbol{\tau}_{drag}$ around pivot point P due to the flow drag and an adhesion and removal torque vector, $\boldsymbol{\tau}_{adh}$ and $\boldsymbol{\tau}_{rem}$ respectively, as can be seen in figure 18. For simplicity a Cartesian coordinate system is used. If the particle is moving to the left the drag force works at a point K on the left hand side of the particle. K is a vector in the Cartesian coordinate system with the origin on the pivot point P. The torque vectors can be expressed in the Cartesian coordinate system as:

$$\boldsymbol{\tau}_{adh} = \boldsymbol{r}_{adh} \times \boldsymbol{F}_{adh} = \begin{pmatrix} -\alpha \\ 0 \\ 0 \end{pmatrix} \times \begin{pmatrix} 0 \\ -F_{adh} \\ 0 \end{pmatrix} = \begin{pmatrix} 0 \\ 0 \\ \alpha F_{adh} \end{pmatrix}, \tag{3.19a}$$

$$\boldsymbol{\tau}_{drag} = \boldsymbol{r}_{drag} \times \boldsymbol{F}_{drag} = \begin{pmatrix} K_x \\ K_y \\ 0 \end{pmatrix} \times \begin{pmatrix} F_{drag} \\ 0 \\ 0 \end{pmatrix} = \begin{pmatrix} 0 \\ 0 \\ -K_y F_{drag} \end{pmatrix}, \tag{3.19b}$$

$$\boldsymbol{\tau}_{rem} = \boldsymbol{r}_{rem} \times \boldsymbol{F}_{rem} = \begin{pmatrix} -\alpha \\ r_p \\ 0 \end{pmatrix} \times \begin{pmatrix} 0 \\ F_{rem} \\ 0 \end{pmatrix} = \begin{pmatrix} 0 \\ 0 \\ -\alpha F_{rem} \end{pmatrix}. \tag{3.19c}$$

It can be seen that if the condition $K_y F_{drag} + \alpha F_{rem} > \alpha F_{adh}$ is true the

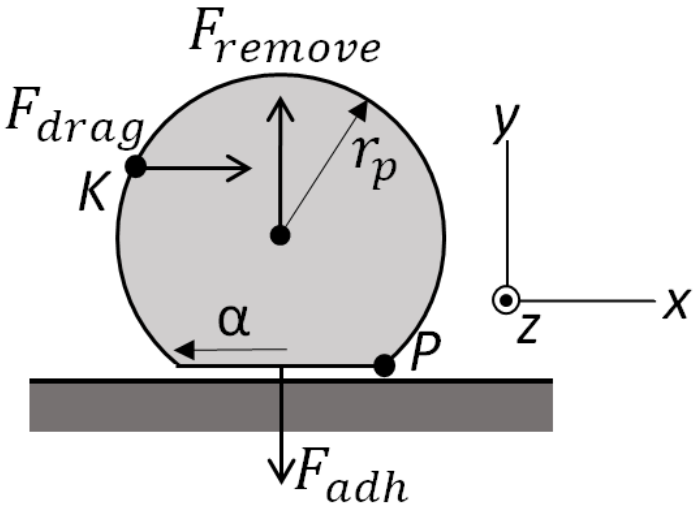

Figure 18: Overview of the forces exerted on the particle. If the particle is moving to the left the drag force will try to rotate the particle clockwise around pivot point P.

particle will start rolling clockwise around the pivot point. The maximum height at which the drag force can be applied to the particle is at

$$K_{y,max} = r_p + \sqrt{r_p^2 - \alpha^2}. \tag{3.20}$$

Using the removal condition and the worst-case scenario of equation 3.20 the ratio T between drag force and removal force can be determined at which the particle will start rolling. This ratio is dependent on the ratio d between α and r_p and on the ratio q between removal force and adhesive force.

$$T = \frac{(\frac{1}{q} - 1)dr_p}{r_p + \sqrt{r_p^2 - d^2 r_p^2}}. \tag{3.21}$$

This equation is plotted for different values of q in figure 19.

It can be seen that if the drag force is much smaller than the removal force rolling will only occur when α is relatively small. The higher q the more the adhesion force is negated by the removal force and rolling will occur at smaller relative drag forces. The figure can be used to determine at which removal force the particle starts rolling, provided the size of the drag force is known. For example we can look at the situation where the

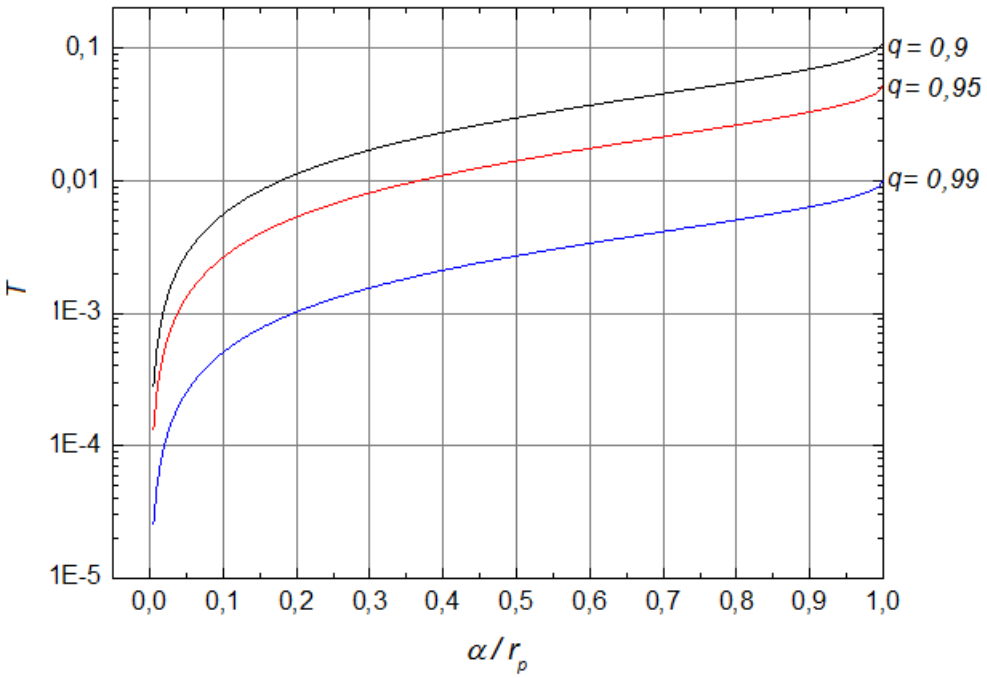

Figure 19: Ratio of drag force to removal force when the particle starts rolling, for a 50 µm particle. The ratio increases as the relative size of the contact radius α increases or the relative size of the removal force decreases.

drag force is three orders of magnitude smaller than the removal force, i.e. $T = 0.001$, and α is a tenth the size of r_p. The particle will have started rolling at $q = 0.99$ but not at $q = 0.95$. The point at which the particle starts rolling greatly depend on the drag force and the particle contact mechanics. However, in the limit $q \to 1$ T will become infinitely small and the roll will occur regardless of the size of α and as long as drag force is not exactly zero. This means rolling of the particle as it approaches removal cannot be prevented but if it occurs very close to the moment of release (high q ratio) it is not of great concern.

4 Conclusion and Outlook

The centrifuge setup with a magnesium disk is a suitable method of measuring the plasma dust removal force and is able, according to the stress analysis, to withstand the extreme force. The gas flow around the disk and particle were simulated and the gas pressure force on the particle was calculated. It was found that this force is several orders of magnitude smaller than the centrifugal force exerted. Changing the pressure, particle radius and rotational speed parameters did not have a significant negative impact on the relative force magnitude. However, extrapolation of these results showed that for typical pressure and rotational speed values the flow force starts to become significant in comparison to the centrifugal force for particle radii smaller than approximately 0.84 μm. This is smaller than the particles that will be used in the experiment. At high pressure levels (> 1 atm) the flow force becomes relatively large. Because pressure does not influence any of the other forces this could be used in a future study to experimentally determine the gas flow force on the particle.

In the experiment rolling of the particle due to gas flow drag will occur at some point as the removal force is being increased. The start of the roll depends on the particle contact mechanics and the intensity of the drag force. To determine when the rolling starts more needs to be known about the area of contact between the particle and the surface. This could be researched further in the future.

5 References

[1] T. E. Flanagan et al.,
Dust release from surfaces exposed to plasma,
Phys. Plasmas 13.12 (2006), pp. 123504-11

[2] N. A. Lammers,
Laser-Induced Shock Wave Cleaning of EUV Photomasks,
Eindhoven University of Technology (2012)

[3] H. Hamaker,
The London-van der Waals attraction between spherical particles,
Physica 4.10 (Oct. 1937)

[4] A. Ragab and S. Eldin Bayoumi,
Engineering Solid Mechanics: Fundamentals and Applications (1999)

[5] V. Vullo and F. Vivio,
Rotors: Stress Analysis and Design (2012)
Conical Disk, pp 103-133

[6] R. Byron Bird et al.,
Transport Phenomena,
Revised 2nd Edition (2007)

[7] COMSOL Multiphysics,
CFD Module Version 4.3 (Build 233)

[8] Sydney Chapman and T. G. Cowling,
The Mathematical Theory of Non-uniform Gases,
3rd edition (1990)

[9] G. G. Stokes,
On the Effect of the Internal Friction of Fluids on the Motion of Pendulums,
Transactions of the Cambridge Philosophical Society, Vol. 9, p.8 (1851)

6 Appendix

6.1 Velocity sensor code

This C++ code is uploaded to an Arduino to control the camera capture and measure disk rotation. The measured rotational frequency is printed to the serial USB connection and can be retrieved on the connected computer.

```
1  int pulsePin = 1; //Analog pin connected to the sensor pulse
       signal
2  int cameraTriggerPin = 4; //Digital pin connected to camera
       trigger signal (= COAX core)
3  int updateFrequency = 1; //Requested updates per second, 0 for
       every single count
4  int countMax = 1; //Counts accumulated until measurement,
       adjusts automatically
5  int markValue = 800; //Maximum sensor value for passing mark
6
7  int count;
8  int analogValue;
9  long lastPulse;
10 long currentPulse;
11 int millisInterval;
12 float pulseFrequency;
13 bool wasOn = false;
14 bool on;
15
16 void setup()
17 {
18   //Set input and output pin modes, start serial connection
19   pinMode(pulsePin,INPUT);
20   pinMode(cameraTriggerPin,OUTPUT);
21   Serial.begin(9600);
22 }
23
24 void triggerCamera()
25 {
26   //Send a small pulse signal to the camera trigger
27   digitalWrite(cameraTriggerPin,HIGH);
28   digitalWrite(cameraTriggerPin,LOW);
29 }
30
31 void loop()
32 {
33   //Read analog input value
34   analogValue = analogRead(pulsePin);
35
36   //Most important line: check if retreived value matches
       condition for passing disk mark
37   on = (analogValue<=markValue);
38
39   if(on && !wasOn) //Only at initial mark detection
40   {
41     wasOn = true;
```

```
42
43      //Increase count and skip until requested amount of counts
44      count += 1;
45      if(count < countMax)
46        return;
47
48      currentPulse = millis();
49
50      if(lastPulse==0)
51      {
52        //Skip first pulse because no frequency can be measured
53        lastPulse = currentPulse;
54        return;
55      }
56
57      triggerCamera();
58
59      //Determine pulse frequency using current and previous pulse
            time and send to pc
60      millisInterval = currentPulse - lastPulse;
61      pulseFrequency = 1000.0f*countMax/millisInterval;
62      Serial.println(pulseFrequency);
63
64      //Estimate amount of counts for requested update frequency.
            If frequency is 0 amount of counts is set to 1.
65      if(updateFrequency!=0)
66      {
67        countMax = pulseFrequency/updateFrequency;
68        if(countMax < 1)
69          countMax = 1;
70      }else{
71        countMax = 1;
72      }
73
74      //Store pulse time and reset count
75      lastPulse = currentPulse;
76      count = 0;
77
78      return;
79    }
80
81    wasOn = on;
82  }
```